



Fiber-based MnO₂/carbon nanotube/polyimide asymmetric supercapacitor



Guangxi Huang^{a, b}, Ye Zhang^a, Lie Wang^a, Peng Sheng^c, Huisheng Peng^{a, *}

^a State Key Laboratory of Molecular Engineering of Polymers, Department of Macromolecular Science, and Laboratory of Advanced Materials, Fudan University, Shanghai, 200438, China

^b Ningguo Long Sheng Flexible Energy Storage Materials Technology Co. Ltd., Ningguo, Anhui 242300, China

^c Material Laboratory of State Grid Corporation of China, State Key Laboratory of Advanced Transmission Technology, Global Energy Interconnection Research Institute, Beijing, 102209, China

ARTICLE INFO

Article history:

Received 7 July 2017

Received in revised form

14 September 2017

Accepted 29 September 2017

Available online 30 September 2017

ABSTRACT

With the development of wearable electronics, fiber-based supercapacitors with both high energy and power densities are under growing demand. Herein we discovered a high performance fiber-based asymmetric supercapacitor (FAS) based on two carbon nanotube (CNT) composite fibers. MnO₂ nano-sheets were *in situ* grown on a CNT fiber to serve as the positive electrode, while polyimide was deposited onto another CNT fiber to form the negative electrode. The resulting aqueous FAS demonstrated broad operating voltage window (0–2.1 V), high areal energy density (36.4 μWh cm⁻² at power density of 0.78 mW cm⁻²) and high power density (15.6 mW cm⁻² at energy density of 30.2 μWh cm⁻²) with good rate performance, long cycling life and high flexibility.

© 2017 Elsevier Ltd. All rights reserved.

1. Introduction

Wearable electronic devices, such as smart watch and intelligent bracelet, are changing the way we live or work at present. However, they still cannot satisfy the application requirements completely. Therefore, the next generation of wearable products including artificial skin, smart fabric and electronic textile have attracted more and more attentions in recent years [1–3]. To achieve the portability and wearability, the development of flexible power sources is a top priority for wearable devices [4–6]. Traditional planar or blocky power systems are too bulky or rigid to use. In contrast, light weight, small volume and good flexibility are the advantages of fiber-based power devices, which can be deformed into various desired shapes and further woven or knitted into textiles to reveal more functions [7–9]. Among various power sources, supercapacitor was deemed as the most promising one for wearable electronic devices due to long cycling life, high power density, fast charge-discharge capability and safe operation [9]. Although a great deal of effort has been devoted for developing fiber-based supercapacitors, they still suffer from lower energy densities compared with traditional planar supercapacitors or

lithium ion batteries [10]. So the main challenge now is to increase the energy densities of the fiber-based supercapacitors without sacrificing their high power densities.

The energy density (E) formula of supercapacitor is $E = CV^2/2$, where C and V represent the specific capacitance and the operating voltage of the total supercapacitor, respectively. That is to say, there are two approaches to improve the energy density of a fiber-based supercapacitor: enhancing the capacitance (C) and enlarging the voltage window (V). The capacitance of supercapacitor is closely related to the electrical conductivity, electrochemical activity and structural stability of electrode materials. Traditional electrical double-layer supercapacitor exhibits poor capacitance, while pseudocapacitor stores much more energy *via* fast and reversible Faradic reactions between electrode and electrolyte. As a result, fiber-shaped electrodes are commonly fabricated by coating pseudocapacitive materials on the metal wire or carbon based fiber. Up to now, various materials including conducting polymers, carbonaceous materials and transition metal oxide/hydroxide have been explored as pseudocapacitive materials in supercapacitors [11–15]. Extending the voltage window is another effective method to increase energy density. Generally, organic electrolytes or ionic liquids can provide higher operating voltages in comparison to water containing electrolytes, but their applications are always constrained by safety problems or price. To overcome the low

* Corresponding author.

E-mail address: penghs@fudan.edu.cn (H. Peng).

operating voltage of aqueous electrolytes, fiber-based asymmetric supercapacitors (FAS) assembled from a battery-like Faradaic positive electrode and a capacitor-like negative electrode are proposed. By integrating the respective advantages of the two different electrodes, asymmetric supercapacitors can extend the voltage window to more than 2 V so as to achieve high energy density.

Herein, we designed and fabricated a high performance FAS made of MnO₂ coated CNT fiber as positive electrode and CNT fiber deposited with polyimide (PI) nanosheets as negative electrode. MnO₂ is widely explored as a pseudocapacitive material for positive electrode due to its outstanding capacitance characteristics [16]. In addition, its low cost, environmental compatibility and natural abundance are also superior than other transition-metal oxides. Nevertheless, its application is restricted by low electrical conductivity and cycling life. To overcome the intrinsic shortage of MnO₂, we adopted highly conductive CNT fiber as the current collector and support to *in situ* grow MnO₂ nanosheets. The obtained MnO₂/CNT fiber served as the positive electrode. To prepare negative electrode based on CNT fiber, PI was employed as the pseudocapacitive material for the first time. PI can store/release energy by the association/disassociation of Li⁺ or Na⁺ ions with four oxygen atoms of the imide group, leading to a high theoretical capacity. *In-situ* polymerized PI can form vertically aligned nanosheets, facilitating the electron transport and ion diffusion in redox reactions [17–19]. In addition, it is thermally stable and mechanically strong. Therefore, PI had been recently explored as anode materials in lithium- and sodium-ion-batteries [17–21]. The assembled FAS showed a large voltage window up to 2.1 V, resulting in both high areal energy density (36.4 μWh cm⁻²) and power density (15.6 mW cm⁻² at 30.2 μWh cm⁻²). Besides, it also exhibited long cycling life, good rate performance and high flexibility. This thin FAS was demonstrated to successfully power an LED, aiming at wearable electronic applications.

2. Experimental section

2.1. Preparation of MnO₂/CNT fiber

To prepare the MnO₂/CNT fiber electrode, CNT fiber was immobilized in 50 mL KMnO₄ aqueous solution (22 mmol/L). Then the solution was heated to 80 °C and refluxed for 3, 6 or 9 h under stirring. The obtained hybrid fiber was rinsed twice with deionized water and ethanol before drying at 80 °C for 6 h.

2.2. Preparation of PI/CNT fiber

Typically, 1,4,5,8-naphthalenetetracarboxylic dianhydride (2.3 mmol) was mixed with *p*-chlorophenol (40 g), followed by the addition of ethylenediamine (0.15 mL) to produce a precursor solution. A CNT fiber that had been fixed on a glass substrate was then immersed in the precursor solution, followed by heating and refluxing for 3, 9 or 12 h. The obtained hybrid fiber was rinsed with ethanol and dried at 300 °C in N₂ for 8 h to remove residual solvent.

2.3. Fabrication of the FAS

The all-solid-state FAS was assembled by employing the MnO₂/CNT and PI/CNT fibers as positive and negative electrodes, respectively, with carboxymethyl cellulose sodium (CMC)/Na₂SO₄ gel as electrolyte and separator. The CMC/Na₂SO₄ gel electrolyte was obtained by mixing 3 g CMC and 6 g Na₂SO₄ in 60 mL deionized water and kept at 80 °C for 2 h under vigorous stirring. MnO₂/CNT and PI/CNT fibers were fixed on a polyethylene terephthalate substrate in parallel. One end of each fiber was pasted with conductive silver adhesive separately. The whole device was then heated up

steadily to 80 °C for 1 h until the conductive silver adhesive had been solidified. CMC/Na₂SO₄ gel electrolyte was finally painted on two fiber electrodes to produce an all-solid-state FAS. The effective length of the FAS was controlled to be 2 cm for electrochemical measurements.

3. Results and discussion

3.1. Characterization of positive electrode

MnO₂/CNT fiber electrode was synthesized through a redox reaction between CNT fiber and KMnO₄, which is a facile method to grow MnO₂ with different nanostructures on various carbonaceous substrates [22]. The reaction followed a stoichiometric equation: 4KMnO₄ + 3C + H₂O → 4MnO₂ + K₂CO₃ + 2KHCO₃, here C is the elemental amorphous carbon associated with CNTs. The bare CNT fibers showed high electrical conductivities from 700 to 1000 S cm⁻¹ with tensile strengths of about 300 MPa. After *in situ* growth of MnO₂, the diameters of the MnO₂/CNT fibers were increased to 142–173 μm (Fig. 1 and Fig. S2), in sharp contrast to 76 μm of the bare CNT fiber (Fig. S1), while the mechanical property was well maintained (Fig. S3). The growing process of MnO₂ nanostructures with different reaction times were characterized by scanning electron microscopy (SEM). After reacted with KMnO₄ for 3 h, a layer of porous MnO₂ composed of a large number of clusters was found to decorate on the surface of CNT fiber (Figs. S2b and S2c). According to the previous study [22–24], MnO₂ nanocrystalline formed at the surface of the CNTs at the initial stage, then they served as the nucleation sites for fresh MnO₂ crystals to deposit and gradually united together to generate nanoclusters. On prolonging the reaction time to 6 h, the morphology of MnO₂ changed a lot (Fig. S2d). MnO₂ clusters interconnected with each other to form vertically arranged nanoflakes, as observed in Fig. 1b and Fig. S2e. This ordered, 3D network structure was beneficial for the electron transport and ion diffusion in redox reactions. With the further increase of the reaction time to 9 h, a large number of blocky MnO₂ with different sizes and different shape were disorderly piled up on the external surface of the fibers (Figs. S2g and S2h). The tightly cumulated state of MnO₂ could be explained below. With the continuous growth of ordered MnO₂ nanosheet arrays, there was not more space to accommodate the newly generated MnO₂. Thus, excess MnO₂ nanoflakes could only be assembled into blocks on the outer surface.

To explore the influence of reaction time on the electrochemical properties of the as-fabricated MnO₂/CNT fiber electrodes, cyclic voltammetry (CV) and galvanostatic charge-discharge tests were carried out in a three-electrode system. Since MnO₂ was instable in an acidic medium, 1 M neutral Na₂SO₄ solution was used as the electrolyte. Fig. S4a compares CV curves of MnO₂/CNT fibers with increasing MnO₂ growth times at 10 mV s⁻¹ within the electrochemical window from 0 to 1.1 V. For a bare CNT fiber, the shape of the curve deviated from the rectangular shape of an ideal capacitor. In contrast, CV curves of MnO₂/CNT fibers were relatively rectangular, indicating a strong supercapacitor nature. As shown in Fig. S4b, although the weight percentage of MnO₂ was continuously increased with increasing growth time from 0 to 9 h, the areal specific capacitance firstly increased and then decreased. The decreasing specific capacitance was mainly derived from the poor electron/ion transport and the increase of resistance after loading too much MnO₂. Therefore, the growth time of 6 h with the MnO₂ weight percentage of 57% was used to optimize the electrochemical properties of the MnO₂/CNT fiber below.

The MnO₂ structures of MnO₂/CNT fiber electrode with a MnO₂ growth time of 6 h were characterized by energy dispersive X-ray spectrometer (EDS) elemental mapping, X-ray diffraction (XRD),

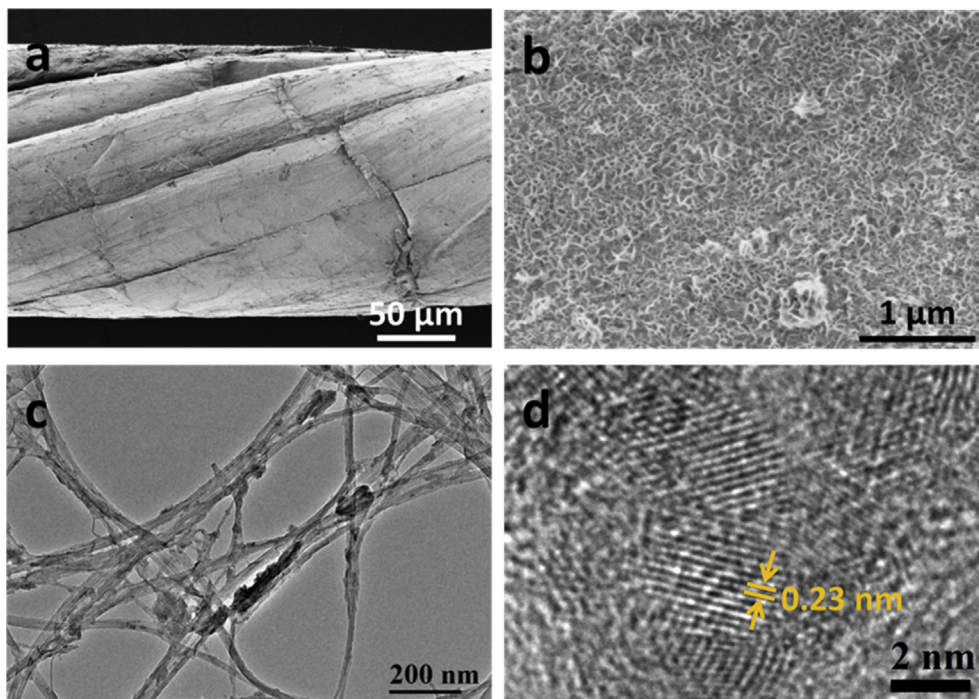


Fig. 1. (a, b) SEM images at low and high magnifications, respectively. (c) TEM and (d) HRTEM images of the MnO₂/CNT fiber with a MnO₂ growth time of 6 h, respectively. (A colour version of this figure can be viewed online.)

Raman and X-ray photoelectron spectroscopy (XPS). The homogeneous distribution of Mn, C and O element throughout the observing area of the MnO₂/CNT fiber was confirmed by EDS (Fig. S5). The crystallographic form of MnO₂ was verified by its XRD pattern. A strong diffraction peak at $2\theta = 25.9^\circ$ which is attributed to the diffraction of (002) lattice plane in graphite from the CNTs was also observed in MnO₂/CNT fiber (Fig. 2a). Two broad diffraction peaks at 36.8° and 66.0° were indexed to the (006) and (119) lattice planes of birnessite-type MnO₂ (JCPDS no. 18-0802), respectively [25,26]. It can be deduced that this sample was at a poorly crystalline state. The Raman spectra of bare CNT and MnO₂/CNT fibers were compared in Fig. 2b. Both of them exhibited all three characteristic Raman bands at 1354 cm^{-1} , 1589 cm^{-1} and 2700 cm^{-1} , corresponding to D, G and G' bands for CNT, respectively [27]. Two bands at 499 cm^{-1} and 571 cm^{-1} in the MnO₂/CNT fiber are ascribed to the major vibration features of MnO₂ compounds, confirming the presence of MnO₂ particles in the hybrid fiber [28,29]. In addition, the relative intensity of D and G bands implied the defect content in CNTs. It can be calculated that the I_D/I_G ratio increased to 0.97 for the hybrid fiber from 0.44 for the bare CNT fiber. The enhancement of defect ratio should be ascribed to the oxidation of CNTs by KMnO₄ during the growth process of MnO₂. The detailed chemical composition of the MnO₂/CNT fiber was determined by XPS spectrum. Signals from Mn, O, and C elements in the full spectrum illustrated the attachment of MnO₂ on the CNT fiber (Fig. S6). As shown in the Mn 2p core level spectrum (Fig. 2c), two binding energy peaks originated from Mn 2p_{3/2} and Mn 2p_{1/2} were located at 642.4 and 654.1 eV, respectively, with an energy separation of 11.7 eV, which were in good agreement with the results reported for MnO₂ [30]. The average oxidation state of Mn was around 3.24 based on the calculation of the area of the peaks associated with Mn-O-Mn and Mn-O-H bonds in O 1s spectrum (Fig. 2d) [31,32]. Therefore, it was composed of both trivalent and tetravalent Mn, which verified the poorly crystalline state of MnO₂ according to the XRD results. Nevertheless, this mixed-valent

system may facilitate the formation of more ionic defects and enhance surface double-layer capacitance during the charge-discharge process [33,34]. The microstructural feature of the MnO₂/CNT fiber was further characterized by transmission electron microscopy (TEM) and high-resolution TEM (HRTEM). Black domains around the CNTs were observed, indicating that MnO₂ flakes could be grown throughout the CNT fiber (Fig. 1c). As shown in the HRTEM image (Fig. 1d), the lattice distance of MnO₂ was measured to be 0.23 nm, corresponding well with the (006) crystal plane of birnessite-type MnO₂ (JCPDS no. 18-0802). This result was in good agreement with the previous XRD data. The nitrogen adsorption/desorption isotherm curve and pore size distribution of MnO₂/CNT fiber with a MnO₂ weight percentage of 60.8% were shown in Fig. S7. The calculated Brunauer-Emmett-Teller (BET) surface area was $106\text{ m}^2\text{ g}^{-1}$.

The effective length, diameter, active working area and weight of the MnO₂/CNT fiber electrode for electrochemical measurements were 2 cm, 170 μm, 0.107 cm² and 210 μg, respectively. Fig. 3a exhibited the CV curves of MnO₂/CNT fiber electrode with a MnO₂ growth time of 6 h at increasing scan rates from 10 to 200 mV s⁻¹. Obviously, the CV curves of the MnO₂/CNT fiber displayed a pair of redox peaks resulting from the reversible faradaic reaction between alkali cations (Na⁺) and MnO₂ nanoflakes according to the following electrochemical reaction: $\text{MnO}_2 + \text{Na}^+ + \text{e}^- \leftrightarrow \text{MnOONa}$ [35]. The intensity of the redox peaks increased with increasing sweep rates. Meanwhile, the rectangular shape of the CV curve had no obvious change, indicating a typical pseudocapacitive behavior of MnO₂ [32]. Fig. 3b showed the charge-discharge curves at various discharge current densities. The nearly symmetric and linear shapes of the curves were maintained, which implied a good reversibility and typical capacitive characteristics of the MnO₂/CNT fiber. On the basis of the charge-discharge curves, the corresponding areal specific capacitances at different discharge current densities were calculated and presented in Fig. 3c. The specific capacitance of the MnO₂/CNT fiber was about 302 mF cm^{-2} at a

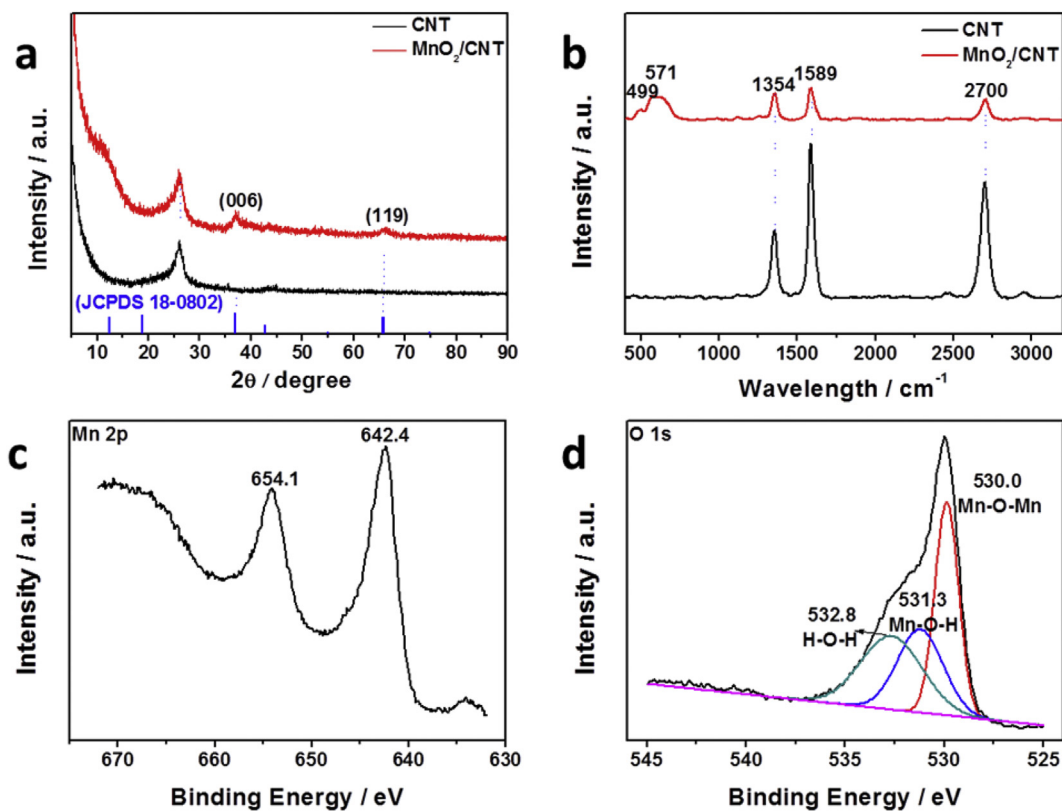


Fig. 2. (a) XRD patterns and (b) Raman spectra of the bare CNT fiber (black line) and MnO_2/CNT fiber (red line). XPS spectra of MnO_2/CNT fiber: (c) Mn 2p and (d) O1s. (A colour version of this figure can be viewed online.)

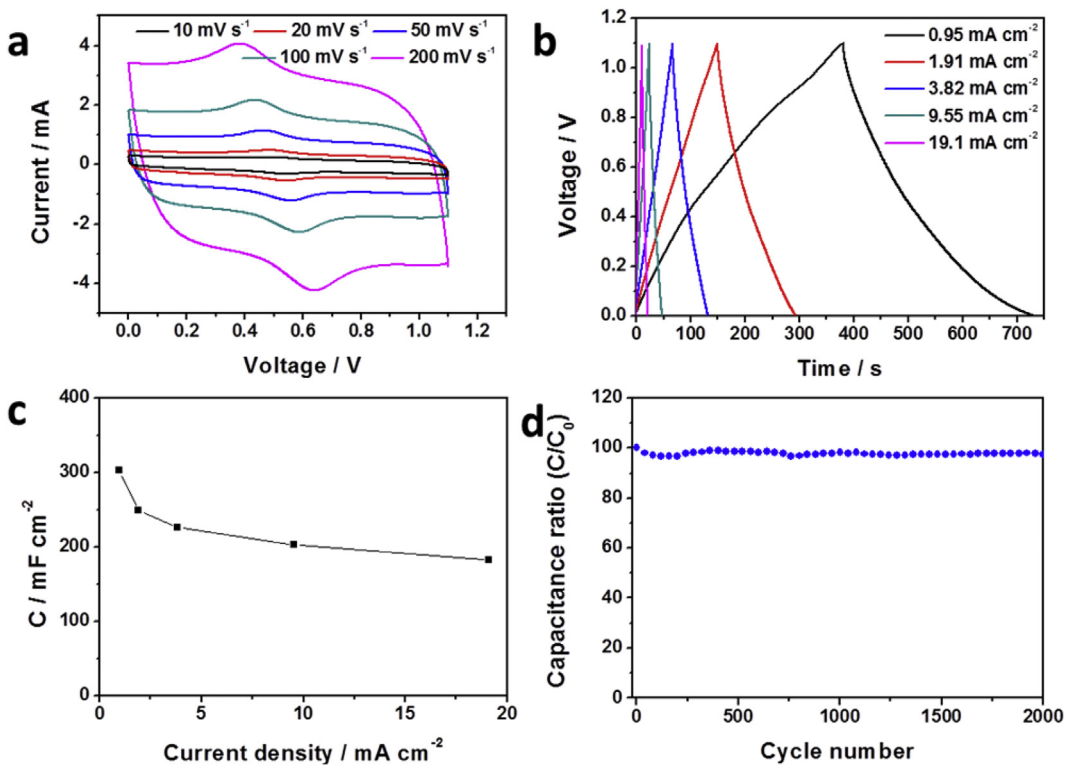


Fig. 3. (a) CV curves of MnO_2/CNT fiber electrode with a MnO_2 growth time of 6 h at increasing scan rates. (b) Charge-discharge curves with increasing current densities. (c) Areal specific capacitance at different current densities. (d) Cycling performance at a current density of 19.1 mA cm^{-2} . (A colour version of this figure can be viewed online.)

current density of 0.95 mA cm^{-2} and still as high as 182 mF cm^{-2} at a current density of 19.1 mA cm^{-2} , which led to a capacitance retention of 60%. The evident decrease of the capacitance was ascribed to a much reduced interior active surface of the MnO_2 accessed by electrolyte ions at high current density [24,36–38]. Besides, charge-discharge cycling tests revealed that 97.3% of the initial specific capacitance was retained after 2000 cycles (Fig. 3d), indicating a good electrochemical stability.

3.2. Characterization of negative electrode

PI/CNT fiber electrode was synthesized by *in situ* polymerization of monomers on the surface of CNTs to form a skin-core structure [19]. Only the two ends of the CNT fiber were fixed to the glass substrate during the reaction, so PI could grow effectively and uniformly at the surface across the fiber. After the formation of PI layer, the diameter of the PI/CNT fibers was increased to 144–194 μm (Fig. 4 and Fig. S8). And the hybrid fiber exhibited a tensile strength of 264 MPa (Fig. S9). SEM images of PI/CNT fiber electrodes collected at different reaction times are shown in Fig. 4 and Fig. S8. For a short polymerization time of 3 h, only small PI nanosheets were deposited on partial surface of the CNT fiber (Figs. S8b and S8c). With the increasing of synthetic time from 3 to 9 h, nanosheets grew larger and denser and CNT fiber was fully covered by PI nanoflakes (Fig. S8d). Numerous PI nanosheets were closely stacked and interconnected laterally to form a highly open and porous structure (Fig. 4 and Fig. S8e), which is favorable for improving the capacitive performance. When the reaction time was further prolonged, the PI nanosheets fused into larger ones and voids between them were reduced (Figs. S8g and S8h).

The electrochemical properties of the as-prepared PI/CNT fiber electrodes with different PI growth times were compared by CV and galvanostatic charge-discharge tests in a three-electrode system with 1 M Na_2SO_4 solution as electrolyte. After the growth of PI nanosheets, PI/CNT fiber electrodes all displayed high

electrochemical activity, while the bare CNT fiber showed almost no response in the voltage range from -1.0 to 0 V (Fig. S10a). We then compared the areal specific capacitance of PI/CNT fibers with increasing PI growth times (Fig. S10b). The specific capacitance and the mass load of PI increased with increasing growth time from 0 to 9 h and then decreased with a further prolongation of growth time, perhaps due to the detachment of PI nanoflakes after refluxing for a relatively long time. Therefore, the growth time of 9 h with the PI weight percentage of 42% was used for the following study.

Infrared spectroscopy was utilized to verify the formation of PI on the CNT fiber (Fig. 5a). Obviously, the new peaks at 766 cm^{-1} and 1703 cm^{-1} were attributed to the formation vibration and asymmetrical vibration of imine $\text{C}=\text{O}$ bond, respectively, while 1350 cm^{-1} was originated from the stretching vibration of imine $\text{C}-\text{N}$ bond of PI [20]. The Raman spectra of bare CNT and PI/CNT fibers were further compared (Fig. 5b). The two peaks at 1350 cm^{-1} and 1585 cm^{-1} are assigned to the D and G bands of CNT, respectively. I_D/I_G ratio increased from 0.44 for bare CNT fiber to 0.50 for hybrid fiber, revealing the formation of chemical bonds between CNT and PI [17]. Fig. 5c displayed the XRD pattern of bare CNT and PI/CNT fibers. A diffraction peak at $2\theta = 17.3^\circ$ and two humps between 25° and 45° were observed in PI/CNT fiber, suggesting that PI had a certain extent of crystallinity. The detailed chemical composition of the PI/CNT fiber was investigated by XPS spectrum. Signals from C, O, and N elements were observed in the full spectrum (Fig. S11a). $\text{C}1\text{s}$ spectrum had the peaks at 284.7, 285.5, 286.3 and 288.8 eV, corresponding to the $\text{C}-\text{C}$ bond, $\text{C}-\text{H}$ bond, $\text{C}-\text{N}$ bond and carbonyl group ($\text{C}=\text{O}$), respectively (Fig. S11b). The peak at 531.9 eV in $\text{O}1\text{s}$ spectrum was derived from carbonyl oxygen ($\text{C}=\text{O}$) (Fig. S11c). $\text{N}1\text{s}$ spectrum displayed only one symmetric peak at 400.7 eV, which was attributed to imide nitrogen ($\text{C}-\text{N}$) (Fig. 5d). All the XPS spectra evidenced the presence of imide unit in the PI/CNT fiber. TEM images of PI/CNT fiber were presented in Fig. 4c and d. PI wrapped around the outer surface of the MWCNT to form a skin-core structure, which was consistent with the SEM results.

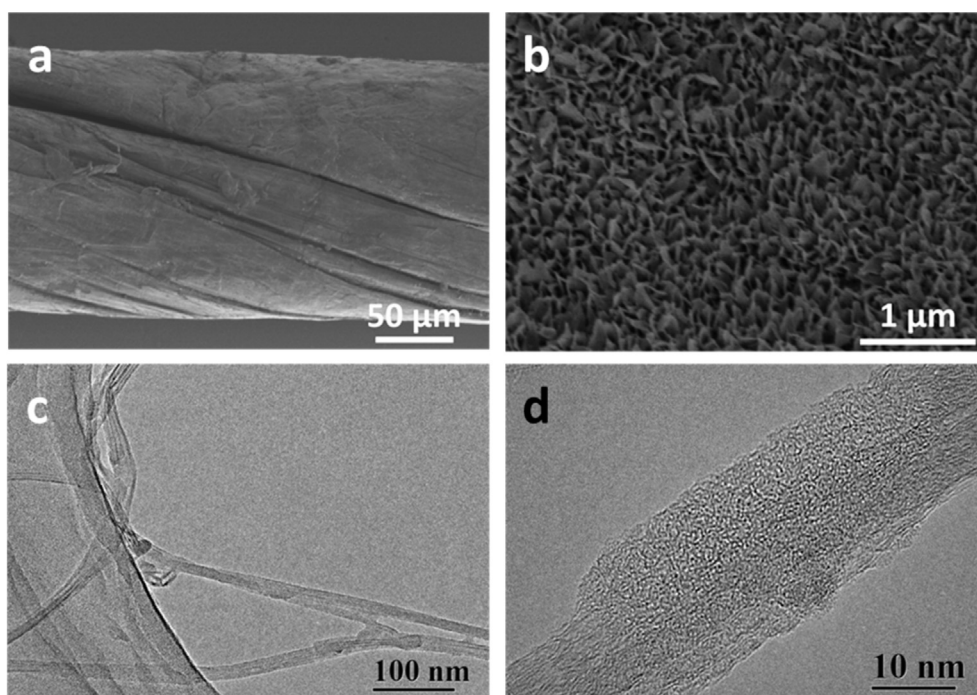


Fig. 4. (a, b) SEM images at low and high magnifications, respectively. (c) TEM and (d) HRTEM images of the PI/CNT fiber with a PI growth time of 9 h, respectively.

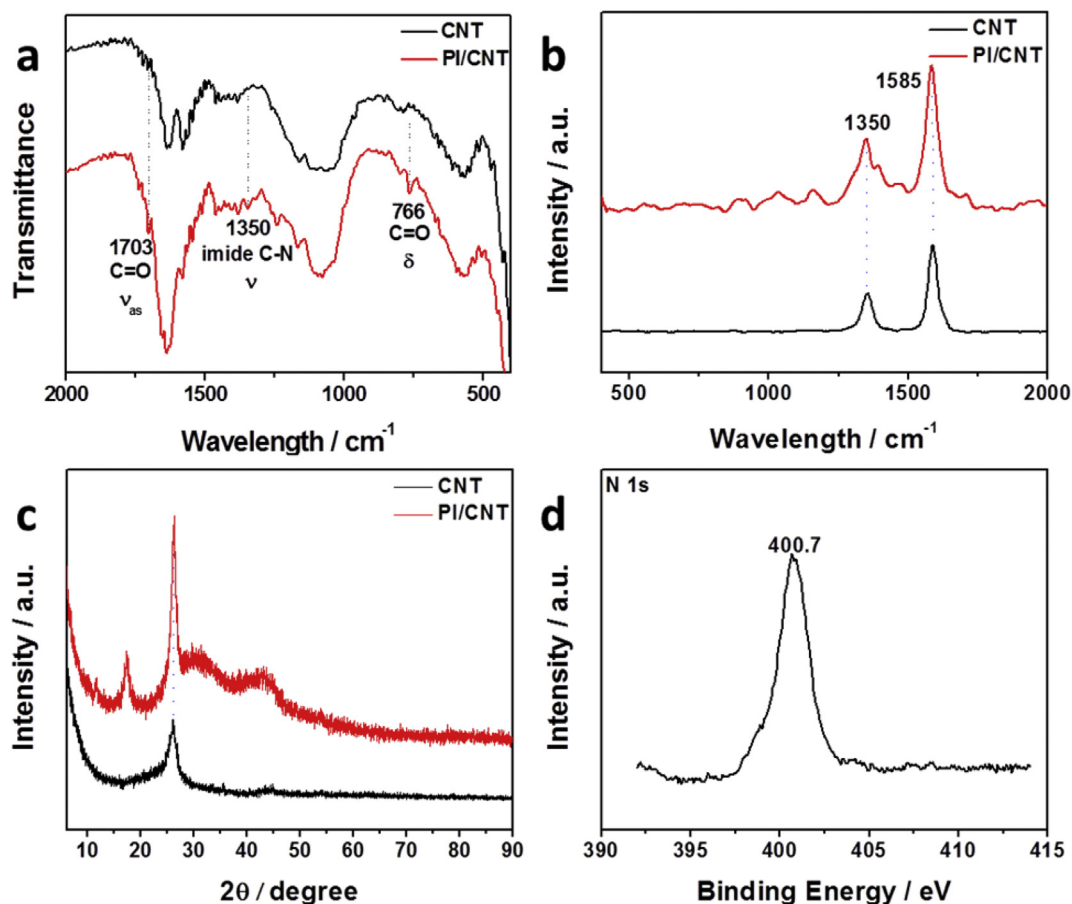


Fig. 5. (a) Infrared spectra, (b) Raman spectra and (c) XRD patterns of the bare CNT fiber (black line) and PI/CNT fiber (red line). (d) XPS spectrum of PI/CNT fiber: N1s. (A colour version of this figure can be viewed online.)

The effective length, diameter, active working area and weight of the PI/CNT fiber electrode for electrochemical measurements were 2 cm, 140 μm , 0.088 cm^2 and 128 μg , respectively. Fig. 6 showed the electrochemical characterizations of PI/CNT fiber electrode with a PI growth time of 9 h. According to previous studies, carbonyl groups in the PI structure can store energy through a two-step redox process, so the CV curves of PI/CNT fiber electrode displayed two pairs of redox peaks (Fig. 6a) [17–21]. During the reduction process, the oxygen atom of the imide group associates with Na^+ to form the radical anion ($\text{PI}^{\cdot-}$) and then the dianion (PI^{2-}) step by step. In the oxidation process, Na^+ is removed and carbonyl groups are recovered, as shown in Fig. S12 [21]. The shape of the CV curves was maintained at increasing scan rates from 10 to 200 mV s^{-1} , indicating a low resistance and good rate performance. Charge-discharge curves of PI/CNT fiber electrode at various current densities were nearly symmetric (Fig. 6b), which demonstrated a high reversibility of the redox reactions of PI. The corresponding areal specific capacitances at different discharge current densities derived from the charge-discharge curves were plotted in Fig. 6c. There was only 14.5% loss for the capacitance when the current density increased to 17.6 mA cm^{-2} (330 mF cm^{-2}) from 0.88 mA cm^{-2} (386 mF cm^{-2}), revealing a good rate capability of PI/CNT fiber. Moreover, the capacitance retention was 96.4% after 2000 consecutive cycles (Fig. 6d). It can be seen that the PI/CNT fiber exhibited good energy storage properties: high specific capacitance, good rate capability and cycle life. As a result, it is a promising negative electrode in FAS.

3.3. Characterization of FAS

The solid-state FAS was fabricated by using MnO_2/CNT and PI/CNT fibers as the positive and negative electrodes, respectively (Fig. S13). To the best of our knowledge, the electrochemical performance of MnO_2 -based supercapacitor may undergo a fast degradation in acid electrolyte due to the dissolution of Mn ion (Mn^{3+} or Mn^{2+}) produced from MnO_2 during discharging process [39,40]. In addition, the neutral gel electrolyte is safer than acidic or basic electrolyte for practical applications. Therefore, CMC/ Na_2SO_4 gel electrolyte was used in this work. In the previous results, MnO_2/CNT positive electrode revealed stable operating voltage within 0–1.1 V, while PI/CNT negative electrode was measured with a potential window from –1 to 0 V. Thus, it was expected that the maximal operation voltage of the as-fabricated FAS can be extended to 2.1 V. In order to maximize the voltage window and specific capacitance of the FAS, positive and negative electrodes should be carefully matched to reach the charge balance, following the relationships of $Q^+ = Q^-$ and $Q = C \times m \times \Delta E$. Here the charge (Q) stored by two electrodes depends on the gravimetric capacitance (C), mass (m) and the potential window for charge-discharge process (ΔE) of positive or negative electrode. According to these equation, the optimal mass ratio of the two electrodes should be $m^+/m^- = 1.44$. Fig. S14 compared the charge-discharge curves of the two electrodes with the optimal mass ratio at a charging current of 0.133 mA. The similar discharge time demonstrated that the two electrodes provided almost the same total charges, thereby the

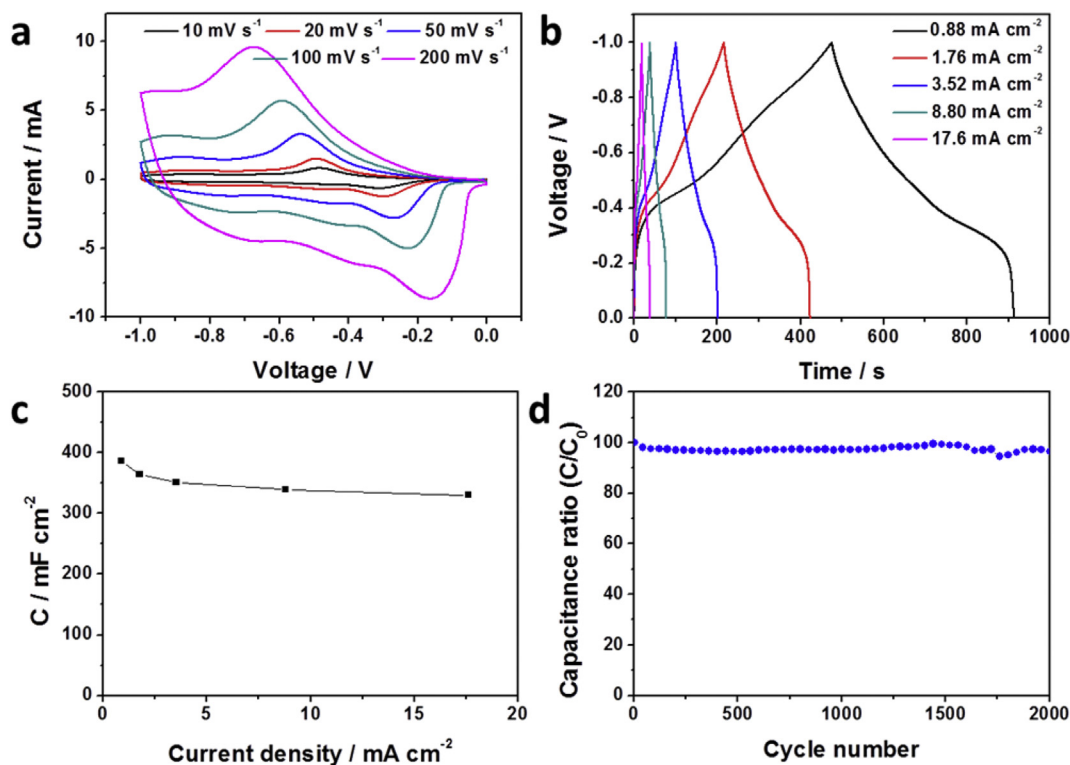


Fig. 6. (a) CV curves of PI/CNT fiber electrode with a PI growth time of 9 h at increasing scan rates. (b) Charge-discharge curves with increasing current densities. (c) Areal specific capacitance at different current densities. (d) Cycling performance at a current density of 17.6 mA cm⁻². (A colour version of this figure can be viewed online.)

charge balance was realized.

Fig. 7 showed the CV curves of the FAS measured at a scan rate of 50 mV s⁻¹ and charge-discharge curves at a current density of 0.74 mA cm⁻² with increasing operation voltages from 1.3 to 2.1 V. The electrochemical behavior of the FAS was different from a regular pseudocapacitor characterized by nearly rectangular CV curves, revealing that the capacitance characteristics of the FAS are mainly derived from the Faradaic redox reaction [41,42]. As expected, the CV and charge-discharge curves of the FAS maintained their shapes in all voltage windows. According to energy density formula, high voltage window is very beneficial for energy storage. When the applied voltage was raised from 1.3 to 2.1 V, the specific capacitance based on the total surface area of positive electrode and negative electrode increased from 32 to 59 mF cm⁻² (Fig. S15). Hence, we further investigated the electrochemical properties of

the FAS within an operating voltage window of 0–2.1 V.

CV curves of the FAS at various scan rates were similar to each other (Fig. 8a). The stable shape of the CV curve even at a scan rate up to 500 mV s⁻¹ suggested highly reversible Faradaic reaction and excellent capacitive performance. Charge-discharge curves of the FAS were conducted with increasing current densities from 0.74 to 14.85 mA cm⁻², as shown in Fig. 8b. The nearly triangular shapes confirmed the high capacitive performance of the FAS. The discharge plateaus in the curves originated from the negative electrode denoted the pseudocapacitive feature. According to the charge-discharge curves, the areal specific capacitances were calculated and summarized in Fig. 8c. The capacitance reached 59.5 mF cm⁻² (32.8 F g⁻¹, based on the total mass of two electrodes without electrolytes) at 0.74 mA cm⁻². When raising the current density up to 14.85 mA cm⁻², a capacitance of 49.2 mF cm⁻²

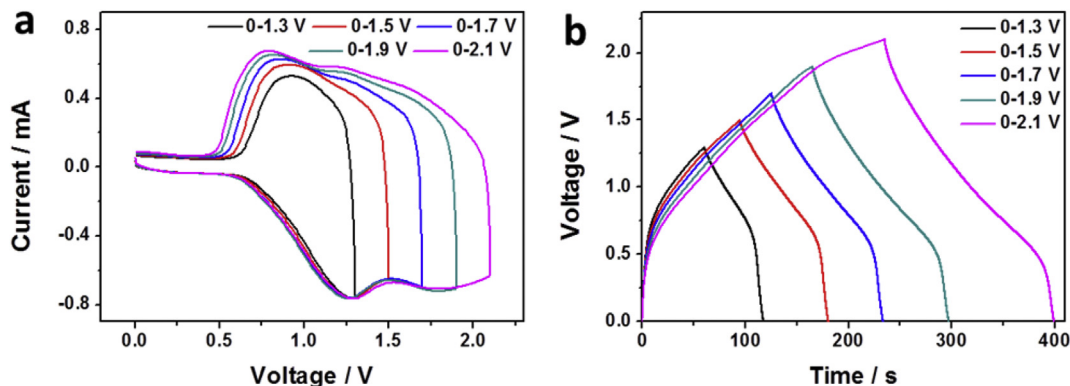


Fig. 7. (a) CV curves of the FAS at a constant scan rate of 50 mV s⁻¹ and (b) charge-discharge curves at a constant current of 0.74 mA cm⁻² collected at different operating voltage windows. (A colour version of this figure can be viewed online.)

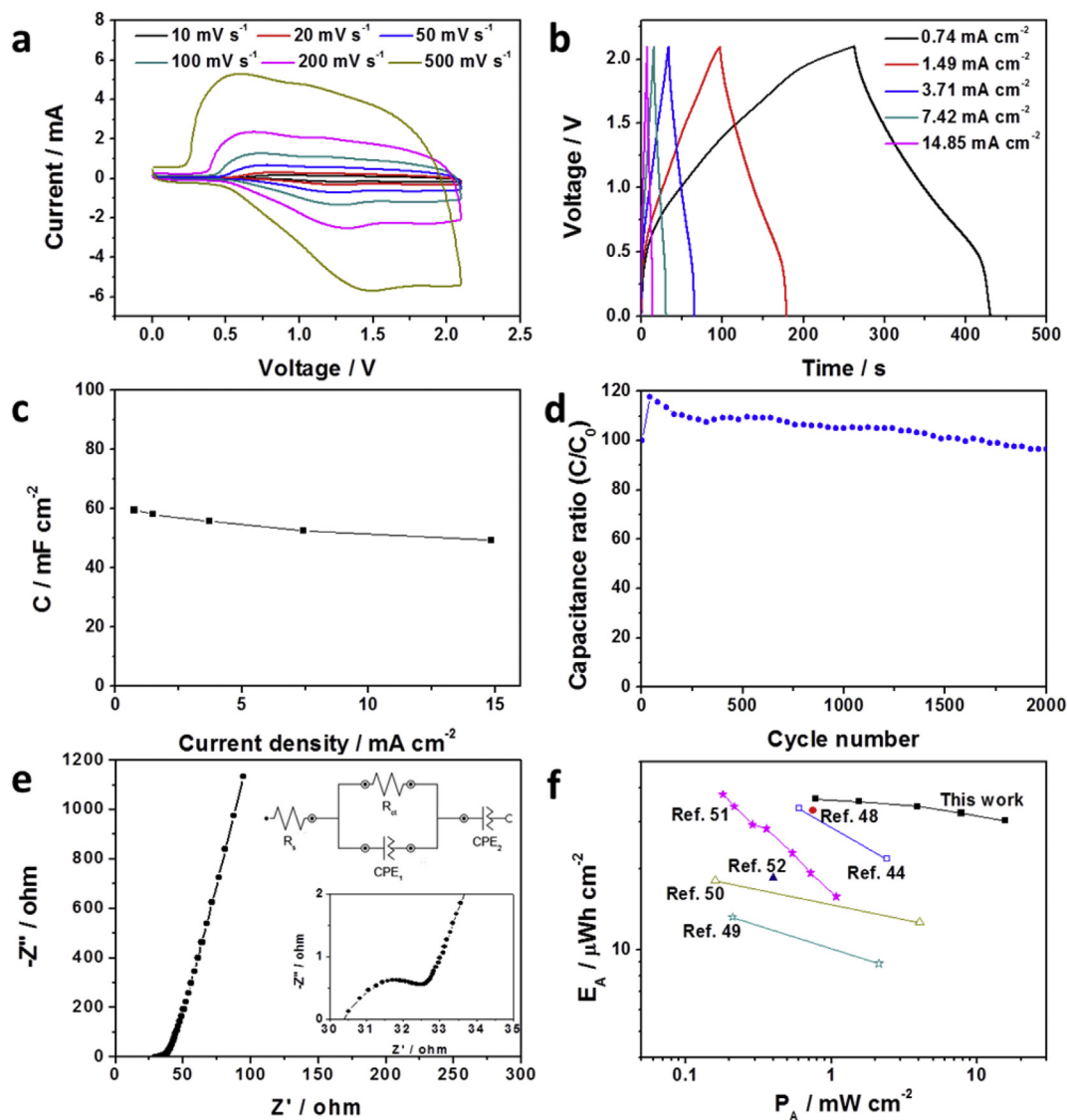


Fig. 8. (a) CV curves of the FAS at increasing scan rates. (b) Charge-discharge curves with increasing current densities. (c) Areal specific capacitance at different current densities. (d) Cycling performance at a current density of 14.85 mA cm^{-2} . (e) Electrochemical impedance spectra with insets showing the high-frequency parts and equivalent circuit diagram used for fitting the EIS data. (f) Ragone plots of our FAS compared with the other reported FASs. (A colour version of this figure can be viewed online.)

(27.1 F g^{-1}) was still achieved, indicating a good rate capability. The FAS also displayed stable cyclic performance (Fig. 8d). The capacitance gradually increased in the first 40 cycles, which may be due to the full activation of the active materials by increased effective interfacial contact between gel electrolyte and electrode materials [41,43,44]. After 2000 charge-discharge cycles, the device kept as much as 96.3% of its initial capacitance. For the prolonged 5000 charge-discharge cycles, the capacitance displayed an apparent attenuation (Fig. S16a). We considered that the degradation of capacitance may be attributed to the structure change caused by the volume expansion/contraction of electroactive materials after repetitious ion intercalation/deintercalation during the charge-discharge process, ultimately leading to the detachment of electroactive materials from CNT fiber [37,38,44]. Electrochemical impedance spectra (EIS) measurement was carried out to study the conductivity and the result was analyzed using Nyquist plots (Fig. 8e). The impedance curve consisted of a near semicircle in the high frequency range, followed by a line in the low frequency. The EIS data were fitted using equivalent circuit model, as shown in the

inset of Fig. 8e. It was found that the FAS had a relatively low solution resistance (R_s) of $30.4 \text{ } \Omega$ and charge transfer resistance (R_{ct}) of $2.9 \text{ } \Omega$ compared to the other CNT fiber supercapacitors [45–47]. After 5000 charge-discharge cycles, R_s and R_{ct} were measured to be $43.2 \text{ } \Omega$ and $2.1 \text{ } \Omega$, respectively (Fig. S16b). Energy and power densities are two important performance parameters of supercapacitors. The high specific capacitance and large operating voltage window of the as-fabricated FAS were expected for both high energy and power densities. The total active working area and mass of the FAS were estimated as 0.188 cm^2 and 0.34 mg , respectively. The Ragone plots showed in Fig. 8f compared the performance of our FAS with other reported FASs. The areal energy density of the whole FAS varied from 36.4 to $30.2 \text{ } \mu\text{Wh} \cdot \text{cm}^{-2}$ when the power density was increased from 0.78 to 15.6 mW cm^{-2} . These results revealed that the performance of our FAS was better than many other reports such as PEDOT@MnO₂//C@Fe₃O₄ FAS (33.5 – $21.78 \text{ } \mu\text{Wh} \cdot \text{cm}^{-2}$ and 0.6 – 2.4 mW cm^{-2}) [44], CNT-NiC(OH)_x//AC FAS ($33.0 \text{ } \mu\text{Wh} \cdot \text{cm}^{-2}$ at 0.75 mW cm^{-2}) [48], CNT@ZnO-NWs@MnO₂//CNT FAS (13.25 – $8.91 \text{ } \mu\text{Wh} \cdot \text{cm}^{-2}$ and

0.21–2.12 mW cm⁻²) [49], MnO₂/RGO//RGO FAS (18.1–12.67 μWh·cm⁻² and 0.16–4.03 mW cm⁻²) [50] and CuHCF/CF//PC@CF FAS (37.88–15.78 μWh·cm⁻² and 0.18–1.08 mW cm⁻²) [51], CF@RGO/MnO₂//CF@TRGO FAS (18.5 μWh·cm⁻² at 0.4 mW cm⁻²) [52]. Alternatively, the results normalized to the total weight of the FAS (20.1–16.6 Wh·kg⁻¹ and 0.43–8.60 kW kg⁻¹) were also higher than those of the reported fiber-based supercapacitors (Fig. S17), attributing to the light weight of CNT fiber and large operating voltage window of the

device.

We further investigated the flexibility and mechanical stability of the FAS. The specific capacitances remained almost unchanged when the device was bent to various degrees of 0–180° (Fig. 9a). In addition, the charge-discharge curves were well overlapped after bending and releasing for 2000 cycles (Fig. 9b). These results suggested that the FAS was of high flexibility and mechanical stability. Furthermore, a red light emitting diode was successfully driven by a tiny FAS (Fig. 9c), demonstrating its potential in flexible power source.

4. Conclusions

In conclusion, we have designed and fabricated a high performance aqueous FAS based on two CNT composite fibers. It displayed a wide voltage region of 0–2.1 V, high areal energy density (36.4 μWh cm⁻² at power density of 0.78 mW cm⁻²) and areal power density (15.6 mW cm⁻² at energy density of 30.2 μWh cm⁻²). In addition, a combined long cycling life, good rate performance and high flexibility was also achieved. It may be promising for a variety of flexible and wearable electronic devices. This work also provides a general and effective paradigm in the development of energy and electronic devices.

Acknowledgements

This work was supported by Ministry of Science and Technology (2016YFA0203302), the National Natural Science Foundation of China (grants 21634003, 51573027, 51403038, 51673043 and 21604012) and Science and Technology Commission of Shanghai Municipality (grants 16JC1400702, 15XD1500400 and 15JC1490200).

Appendix A. Supplementary data

Supplementary data related to this article can be found at <https://doi.org/10.1016/j.carbon.2017.09.103>.

References

- [1] K. Cherenack, C. Zysset, T. Kinkeldei, N. Münzenrieder, G. Tröster, Woven electronic fibers with sensing and display functions for smart textiles, *Adv. Mater.* 22 (2010) 5178–5182.
- [2] W. Weng, P. Chen, S. He, X. Sun, H. Peng, Smart electronic textiles, *Angew. Chem. Int. Ed.* 55 (2016) 6140–6169.
- [3] P. Gould, Textiles gain intelligence, *Mater. Today* 6 (2003) 38–43.
- [4] F.R. Fan, W. Tang, Z.L. Wang, Flexible nanogenerators for energy harvesting and self-powered electronics, *Adv. Mater.* 28 (2016) 4283–4305.
- [5] L. Sun, X. Wang, Y. Wang, Q. Zhang, Roles of carbon nanotubes in novel energy storage devices, *Carbon* 122 (2017) 462–474.
- [6] W. Liu, M.-S. Song, B. Kong, Y. Cui, Flexible and stretchable energy storage: recent advances and future perspectives, *Adv. Mater.* 29 (2017) 1603436.
- [7] Y. Zhang, Y. Zhao, J. Ren, W. Weng, H. Peng, Advances in wearable fiber-shaped lithium-ion batteries, *Adv. Mater.* 28 (2016) 4524–4531.
- [8] J. Di, X. Zhang, Z. Yong, Y. Zhang, D. Li, R. Li, et al., Carbon-nanotube fibers for wearable devices and smart textiles, *Adv. Mater.* 28 (2016) 10529–10538.
- [9] D. Yu, Q. Qian, L. Wei, W. Jiang, K. Goh, J. Wei, et al., Emergence of fiber supercapacitors, *Chem. Soc. Rev.* 44 (2015) 647–662.
- [10] J. Yan, Q. Wang, T. Wei, Z. Fan, Recent advances in design and fabrication of electrochemical supercapacitors with high energy densities, *Adv. Energy Mater.* 4 (2014) 5166–5180.
- [11] Z. Yu, L. Tetard, L. Zhai, J. Thomas, Supercapacitor electrode materials: nanostructures from 0 to 3 dimensions, *Energy Environ. Sci.* 8 (2015) 702–730.
- [12] C. Zhang, B. Anasori, A. Seral-Ascaso, S.-H. Park, N. McEvoy, A. Shmeliov, et al., Transparent, flexible, and conductive 2D titanium carbide (MXene) films with high volumetric capacitance, *Adv. Mater.* (2017) 1702678.
- [13] K. Krishnamoorthy, P. Pazhamalai, S. Sahoo, S.-J. Kim, Titanium carbide sheet based high performance wire type solid state supercapacitors, *J. Mater. Chem. A* 5 (2017) 5726–5736.
- [14] M.R. Lukatskaya, S. Kota, Z. Lin, M.-Q. Zhao, N. Shpigel, M.D. Levi, et al., Ultra-high-rate pseudocapacitive energy storage in two-dimensional transition metal carbides, *Nat. Energy* 2 (2017) 17105.

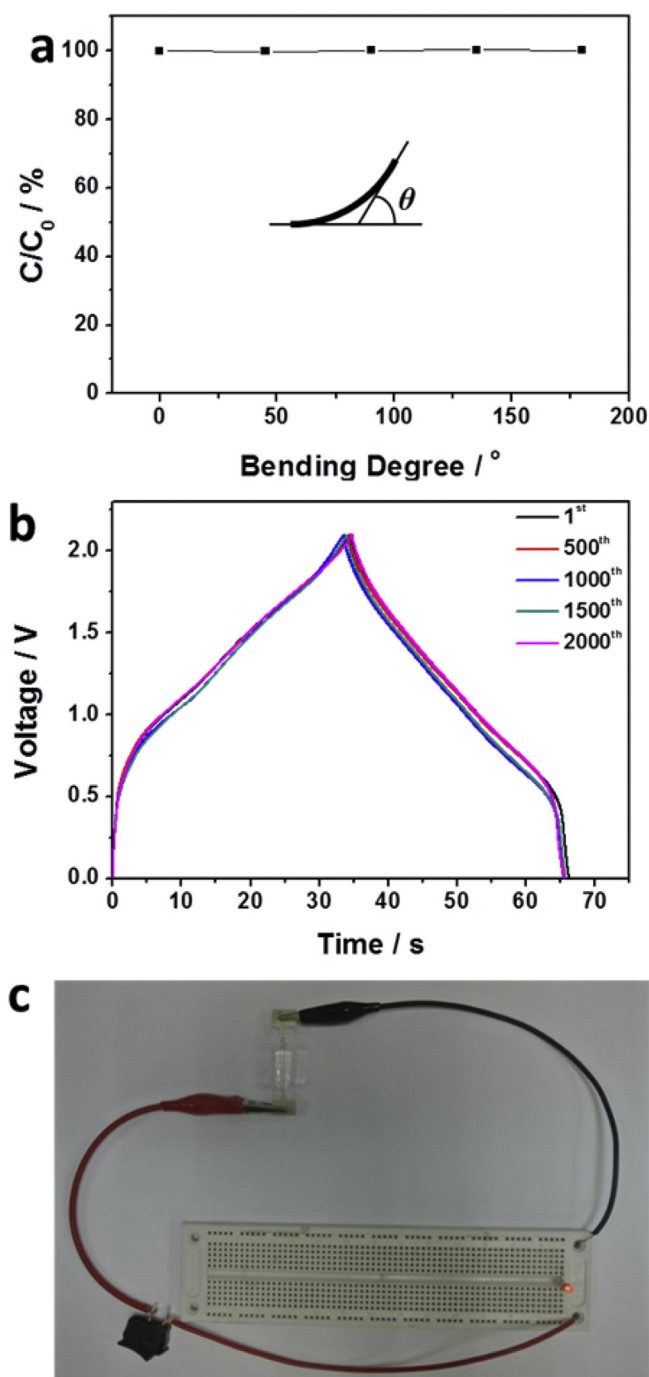


Fig. 9. (a) Capacitance retention of the FAS under different bending angles. (b) Charge-discharge curves before and after bending for 2000 times. (c) Photograph of a red light emitting diode powered by a 2 cm long FAS. (A colour version of this figure can be viewed online.)

- [15] K. Krishnamoorthy, P. Pazhamalai, S.J. Kim, Ruthenium sulfide nanoparticles as a new pseudocapacitive material for supercapacitor, *Electrochim. Acta* 227 (2017) 85–94.
- [16] M. Huang, F. Li, F. Dong, Y.X. Zhang, L.L. Zhang, MnO₂-based nanostructures for high-performance supercapacitors, *J. Mater. Chem. A* 3 (2015) 21380–21423.
- [17] Y. Wang, X. Cui, Y. Zhang, L. Zhang, X. Gong, G. Zheng, Achieving high aqueous energy storage via hydrogen-generation passivation, *Adv. Mater.* 28 (2016) 7626–7632.
- [18] H. Wu, S.A. Shevlin, Q. Meng, W. Guo, Y. Meng, K. Lu, et al., Flexible and binder-free organic cathode for high-performance lithium-ion batteries, *Adv. Mater.* 26 (2014) 3338–3343.
- [19] Y. Zhang, Y. Wang, L. Wang, C.-M. Lo, Y. Zhao, Y. Jiao, et al., A fiber-shaped aqueous lithium ion battery with high power density, *J. Mater. Chem. A* 4 (2016) 9002–9008.
- [20] Z. Song, H. Zhan, Y. Zhou, Polyimides: promising energy-storage materials, *Angew. Chem. Int. Ed.* 49 (2010) 8444–8448.
- [21] W. Deng, Y. Shen, J. Qian, H. Yang, A polyimide anode with high capacity and superior cyclability for aqueous Na-ion batteries, *Chem. Commun.* 51 (2015) 5097–5099.
- [22] X. Jin, W. Zhou, S. Zhang, G.Z. Chen, Nanoscale microelectrochemical cells on carbon nanotubes, *Small* 3 (2007) 1513–1517.
- [23] H. Xia, M. Lai, L. Lu, Nanoflaky MnO₂/carbon nanotube nanocomposites as anode materials for lithium-ion batteries, *J. Mater. Chem.* 20 (2010) 6896–6902.
- [24] W. Dang, C. Dong, Z. Zhang, G. Chen, Y. Wang, H. Guan, Self-grown MnO₂ nanosheets on carbon fiber paper as high-performance supercapacitors electrodes, *Electrochim. Acta* 217 (2016) 16–23.
- [25] S. Devaraj, N. Munichandraiah, Effect of crystallographic structure of MnO₂ on its electrochemical capacitance properties, *J. Phys. Chem. C* 112 (2008) 4406–4417.
- [26] K. Zhang, H. Zhao, Z. Zhang, J. Chen, X. Mu, X. Pan, et al., Cooperative effect of hierarchical carbon nanotube arrays as facilitated transport channels for high-performance wire-based supercapacitors, *Carbon* 95 (2015) 746–755.
- [27] X. Xie, L. Gao, Characterization of a manganese dioxide/carbon nanotube composite fabricated using an in situ coating method, *Carbon* 45 (2007) 2365–2373.
- [28] A. Ogata, S. Komaba, R. Baddour-Hadjean, J.P. Pereira-Ramos, N. Kumagai, Doping effects on structure and electrode performance of K-birnessite-type manganese dioxides for rechargeable lithium battery, *Electrochim. Acta* 53 (2008) 3084–3093.
- [29] Y. Chen, Y. Zhang, D. Geng, R. Li, H. Hong, J. Chen, et al., One-pot synthesis of MnO₂/graphene/carbon nanotube hybrid by chemical method, *Carbon* 49 (2011) 4434–4442.
- [30] J. Yan, Z. Fan, T. Wei, J. Cheng, B. Shao, K. Wang, et al., Carbon nanotube/MnO₂ composites synthesized by microwave-assisted method for supercapacitors with high power and energy densities, *J. Power Sources* 194 (2009) 1202–1207.
- [31] Y. Hou, Y. Cheng, T. Hobson, J. Liu, Design and synthesis of hierarchical MnO₂ nanospheres/carbon nanotubes/conducting polymer ternary composite for high performance electrochemical electrodes, *Nano Lett.* 10 (2010) 2727–2733.
- [32] M. Toupin, T. Brousse, D. Bélanger, Charge storage mechanism of MnO₂ electrode used in aqueous electrochemical capacitor, *Chem. Mater.* 16 (2004) 3184–3190.
- [33] M.-K. Song, S. Cheng, H. Chen, W. Qin, K.-W. Nam, S. Xu, et al., Anomalous pseudocapacitive behavior of a nanostructured, mixed-valent manganese oxide film for electrical energy storage, *Nano Lett.* 12 (2012) 3483–3490.
- [34] M. Kim, J. Kim, Redox deposition of birnessite-type manganese oxide on silicon carbide microspheres for use as supercapacitor electrodes, *ACS Appl. Mater. Interfaces* 6 (2014) 9036–9045.
- [35] O. Ghodbane, J.-L. Pascal, F. Favier, Microstructural effects on charge-storage properties in MnO₂-based electrochemical supercapacitors, *ACS Appl. Mater. Interfaces* 1 (2009) 1130–1139.
- [36] J. Wang, Y. Yang, Z. Huang, F. Kang, A high-performance asymmetric supercapacitor based on carbon and carbon–MnO₂ nanofiber electrodes, *Carbon* 61 (2013) 190–199.
- [37] Z. Lei, F. Shi, L. Lu, Incorporation of MnO₂-coated carbon nanotubes between graphene sheets as supercapacitor electrode, *ACS Appl. Mater. Interfaces* 4 (2012) 1058–1064.
- [38] M. Pang, G. Long, S. Jiang, Y. Ji, W. Han, B. Wang, et al., One pot low-temperature growth of hierarchical δ-MnO₂ nanosheets on nickel foam for supercapacitor applications, *Electrochim. Acta* 161 (2015) 297–304.
- [39] H. Jin, L. Zhou, C.L. Mak, H. Huang, W.M. Tang, H.L. Wa Chan, Improved performance of asymmetric fiber-based micro-supercapacitors using carbon nanoparticles for flexible energy storage, *J. Mater. Chem. A* 3 (2015) 15633–15641.
- [40] Q. Zhu, K. Liu, J. Zhou, H. Hu, W. Chen, Y. Yu, Design of a unique 3D-nanostructure to make MnO₂ work as supercapacitor material in acid environment, *Chem. Eng. J.* 321 (2017) 554–563.
- [41] C. Yuan, J. Li, L. Hou, X. Zhang, L. Shen, X.W. Lou, Ultrathin mesoporous NiCo₂O₄ nanosheets supported on Ni foam as advanced electrodes for supercapacitors, *Adv. Funct. Mater.* 22 (2012) 4592–4597.
- [42] H. Xu, X. Hu, H. Yang, Y. Sun, C. Hu, Y. Huang, Flexible asymmetric micro-supercapacitors based on Bi₂O₃ and MnO₂ nanoflowers: larger areal mass promises higher energy density, *Adv. Energy Mater.* 5 (2015) (n/a–n/a).
- [43] Z. Fan, J. Yan, L. Zhi, Q. Zhang, T. Wei, J. Feng, et al., A three-dimensional carbon nanotube/graphene sandwich and its application as electrode in supercapacitors, *Adv. Mater.* 22 (2010) 3723–3728.
- [44] J. Sun, Y. Huang, C. Fu, Y. Huang, M. Zhu, X. Tao, et al., A high performance fiber-shaped PEDOT/MnO₂/C/Fe₃O₄ asymmetric supercapacitor for wearable electronics, *J. Mater. Chem. A* 4 (2016) 14877–14883.
- [45] X. Cheng, J. Zhang, J. Ren, N. Liu, P. Chen, Y. Zhang, et al., Design of a hierarchical ternary hybrid for a fiber-shaped asymmetric supercapacitor with high volumetric energy density, *J. Phys. Chem. C* 120 (2016) 9685–9691.
- [46] B. Wang, X. Fang, H. Sun, S. He, J. Ren, Y. Zhang, et al., Fabricating continuous supercapacitor fibers with high performances by integrating all building materials and steps into one process, *Adv. Mater.* 27 (2015) 7854–7860.
- [47] Z. Lu, Y. Chao, Y. Ge, J. Foroughi, Y. Zhao, C. Wang, et al., High-performance hybrid carbon nanotube fibers for wearable energy storage, *Nanoscale* 9 (2017) 5063–5071.
- [48] X. Lu, Y. Bai, R. Wang, J. Sun, A high-performance flexible and weavable asymmetric fiber-shaped solid-state supercapacitor enhanced by surface modifications of carbon fibers with carbon nanotubes, *J. Mater. Chem. A* 4 (2016) 18164–18173.
- [49] Y. Li, X. Yan, X. Zheng, H. Si, M. Li, Y. Liu, et al., Fiber-shaped asymmetric supercapacitors with ultrahigh energy density for flexible/wearable energy storage, *J. Mater. Chem. A* 4 (2016) 17704–17710.
- [50] Z. Zhang, F. Xiao, S. Wang, Hierarchically structured MnO₂/graphene/carbon fiber and porous graphene hydrogel wrapped copper wire for fiber-based flexible all-solid-state asymmetric supercapacitors, *J. Mater. Chem. A* 3 (2015) 11215–11223.
- [51] S.T. Senthilkumar, J. Kim, Y. Wang, H. Huang, Y. Kim, Flexible and wearable fiber shaped high voltage supercapacitors based on copper hexacyanoferrate and porous carbon coated carbon fiber electrodes, *J. Mater. Chem. A* 4 (2016) 4934–4940.
- [52] Z. Zhang, F. Xiao, J. Xiao, S. Wang, Functionalized carbonaceous fibers for high performance flexible all-solid-state asymmetric supercapacitors, *J. Mater. Chem. A* 3 (2015) 11817–11823.